Viscosity and Structural Alteration of a Coarse-Grained Model of Polystyrene under Steady Shear Flow Studied by Reverse Nonequilibrium Molecular Dynamics

Xiaoyu Chen,*,† Paola Carbone,† Welchy L. Cavalcanti,‡ Giuseppe Milano,§ and Florian Müller-Plathe†

Technische Universität Darmstadt, Petersenstrasse 20, D-64287 Darmstadt, Germany, Bremen Center for Computational Materials Science, Universität Bremen, Germany, and Department of Chemistry, University of Salerno, Salerno, Italy

Received March 24, 2007; Revised Manuscript Received July 7, 2007

ABSTRACT: The reverse nonequilibrium molecular dynamics (RNEMD) method is implemented to predict the viscosity of a coarse-grained model of short-chain polystyrene. The coarse-grained model has been derived to reproduce the structure of polystyrene. It is therefore not a generic model, but polymer-specific. Here, its performance for dynamical quantities is tested. The zero-shear viscosity is compared with experimental data. The pronounced difference can be mainly attributed to the inherent dynamic properties of the coarse-grained model. The qualitative results are compared to previous results calculated via conventional nonequilibrium molecular dynamics (NEMD) and more generic polymer models, and the agreement is reasonable. The structural alterations under shear are investigated by characterizing the molecular deformation and birefringence extinction angle.

1. Introduction

In the last two decades, several simulation methods for the prediction of shear viscosities have been proposed. In equilibrium molecular dynamics (EMD), the shear viscosity is obtained from pressure or momentum fluctuations based on the Einstein and Green−Kubo relations;[1] In conventional nonequilibrium molecular dynamics (NEMD),[2] the shear viscosity can be calculated by reproducing the experimental setup, i.e., an appropriate perturbation is applied, the ensemble averages of the resulting flux and the corresponding field are measured, the ratio of flux and field gives the shear viscosity. The most widely used NEMD methods are homogeneous shear (HS) and surface-driven shear methods (SD). In the HS method, the shear flow is imposed by modifying the equation of motion of the molecules and using sliding-wall periodic boundary conditions. In the SD method, the shear is imparted on the fluid through the actual motion of the confining walls. A comparison of the applicability, accuracy, and efficiency for these methods can be found in ref 3.

A more recent alternative is the reverse nonequilibrium molecular dynamics (RNEMD) method,[4,5] which is used here. It reverses the experimental cause-and-effect picture: the momentum flux (stress) is imposed by a Maxwell daemon and the corresponding field (velocity gradient) is measured. Compared to the more traditional NEMD techniques, RNEMD offers certain advantages but also has its shortcomings. They have been discussed in more detail elsewhere.[5] Its chief advantage is the fact that no energy is deposited into the simulation, in contrast to other NEMD methods, and hence no energy need be removed by an external thermostat. As most thermostats interfere with the linear momentum, they are a potential error source in viscosity calculations. Further advantages are the absence of boundary regions (as in SD method), the ease of implementation and analysis, and parallelisability.[6] The major shortcoming of RNEMD is that the temperature in the system is not uniform but develops a stationary quadratic profile.[4] As a consequence, the density is also not uniform, so that the calculated viscosity is an average over different temperatures and densities. This aspect requires great care in designing the perturbation to be small enough for these variations to be numerically irrelevant. As one usually attempts anyway in NEMD to make the perturbation as small as possible, in order to have linear-response conditions, this is not a serious restriction, but more a point to be watched. RNEMD has been very successfully applied to predict the viscosity of Lennard-Jones liquids,[4] atomistic models of molecular liquids,[7] simplified models of amphiphiles,[8] liquid crystals,[9] and Yukawa liquids.[10] In particular, ref 10 shows that, for small shear rates, the viscosity values calculated via RNEMD and NEMD simulations are mutually consistent and also in agreement with equilibrium MD calculations. So far, the RNEMD method has not been tried for the calculation of *polymer* viscosities.

The viscosities of polymer melts and structural changes under shear flow are of great practical importance in manufacturing and processing of polymers. Viscosity and structure of polymer melts under shear were intensively studied by conventional NEMD in previous work. Among these studies, some simple and general models have successfully captured the rheological properties and contributed to the understanding of their physical origin.[11−15] A detailed review on simple models for complex nonequilibrium fluids can be found in ref 16. However, the generic models have not been designed to provide quantitative properties of *specific* polymer melts. Some studies on specific macromolecules, which were based on realistic models, have also been carried out.[17−19] The presence of many different time and length scales and the associated computational costs usually preclude the use of fully atomistic force fields. One, therefore, tries to find a coarse-grained (CG) model at a level between atomistic and generic. It should be detailed enough to be

* Corresponding author. E-mail: x.chen@theo.chemie.tu-darmstadt.de. Telephone: +49-6151-16-7315. Fax +49-6151-16-6526. Address: Eduard-Zintl-Institut für Anorganische und Physikalische Chemie, Technische Universität Darmstadt, Petersenstrasse20 D-64287 Darmstadt, Germany.
† Technische Universität Darmstadt.
‡ Present address: Bremen Center for Computational Materials Science.
§ Department of Chemistry, University of Salerno.

10.1021/ma0707178 CCC: $37.00
Published on Web 09/29/2007

material-specific and simple enough to be computationally viable. One way to approach the problem is to reduce the degrees of freedom by coarsening the models, keeping only those degrees of freedom deemed relevant for the particular properties of interest. Parametrization of coarse-grained force fields can be roughly classified into two different approaches. In the first, both static and dynamics properties are used to develop the force field, and the dynamics is matched by an appropriate selection of friction constant appearing in Langevin's equations of motion at the coarse-grained scale.[20,21] In the second approach, only static properties are utilized in the force field parametrization and Newton's equations of motion are used to evolve the system.[22,23] The coarse-grained models developed from this approach can accurately describe the static properties, while on the other hand, the dynamics is generally too fast.[24] In some cases, it was possible to recover the dynamical properties by appropriate time scaling.[25] The dynamical properties predicted by such CG model are based on the philosophy that the same basic mechanisms are still operative at a different time rate when the molecular mobility changes. Therefore, the accelerated dynamics is expected to retain some reality of the motion in the system. Ideally, one would like structurally optimized models to also be able to predict polymer viscosities without any further calibration. Finding out whether this is possible is one aspect of the current investigation.

The aim of this paper is therefore twofold. First, the applicability of the RNEMD algorithm to the prediction of the viscosity of polymers is investigated. We compare the shear behavior to previous studies of similar models, where conventional NEMD methods have been used. Second, we study the rheological behavior of the specific, *realistic* coarse-grained model of polystyrene, which has been developed by taking only structural information into account. For the shortest polymer chain, the zero-shear viscosity is compared to recent experimental results. The material functions (first and second normal stress difference) are briefly discussed and structural properties of polystyrene under shear are also quantitatively characterized in this work.

2. Reverse Nonequilibrium Molecular Dynamics

The RNEMD method for calculating shear viscosity is briefly reviewed in this section, for details, see refs 4 and 5. The shear viscosity η relates the transverse momentum flux $j_z(p_x)$ and the flow velocity gradient $\partial\bar{v}_x/\partial z$ via eq 1

$$j_z(p_x) = -\eta \frac{\partial \bar{v}_x}{\partial z} \tag{1}$$

The magnitude of momentum flux $|j_z(p_x)|$ is equal to the off-diagonal (xz) component of the stress tensor τ_{xz}, and $\partial\bar{v}_x/\partial z$ is also called the shear rate $\dot{\gamma}$. The momentum flux $j_z(p_x)$ can be described as a transport through a surface perpendicular to its direction within a certain time. In RNEMD, $j_z(p_x)$ is imposed in an unphysical way, and the flow field corresponds to two symmetric planar Couette flows, with a shear flow in the x direction and the velocity gradient in the z direction, as illustrated in Figure 1. The orthorhombic simulation cell with size of L_x, L_y, L_z in the periodic system is partitioned into an even number of slabs, here 20, in z direction. One selects in slab 1 the atom with the *largest* negative x component of momentum (mv_{x1}), and in the central slab (slab 11), the atom with the *largest* positive x component of momentum (mv_{x2}). These two atoms must have the same mass m. One exchanges the x component of the velocity vector between these two atoms. As the two atoms have the same mass m, the unphysical momentum swap

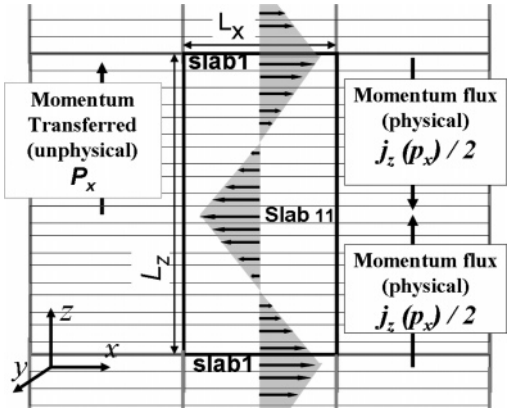

Figure 1. Sketch of the RNEMD method for calculating the shear viscosity. The flow field imposed on the system corresponds to two symmetric planar Couette flows, which have the shear flow in the x direction, and the velocity gradient is in z direction. Horizontal arrows in the simulation cell indicate the velocity field. The periodic orthorhombic simulation cell with size of L_x, L_y, and L_z ($L_x = L_y = L_z/3$) in periodic system is partitioned into 20 slabs in z direction. For details, see text.

conserves both the total linear momentum and the total kinetic energy. The exchanged quantity Δp_x is the x component of the momentum,

$$\Delta p_x = mv_{x1} - mv_{x2} \tag{2}$$

By such velocity swap, momentum (Δp_x) is transferred unphysically across the system. The velocity swap is performed every W time steps, so the time elapsed between two velocity swaps is $W\cdot\Delta t$, with Δt being the length of the time step. The total transferred momentum during the simulation is given by $p_x = \sum\Delta p_x$. The response of the system to this nonequilibrium perturbation is a momentum flux $j_z(p_x)$ in the opposite direction via a physical mechanism, the friction. In the steady state, the unphysical and the physical momentum flux are balanced, and $j_z(p_x)$ can be evaluated by eq 3

$$j_z(p_x) = \frac{p_x}{2tL_xL_y} \tag{3}$$

The factor 2 arises because of the periodicity of the system, and t is the duration of the simulation. The momentum flux $j_z(p_x)$ leads to a continuous velocity gradient $\partial\bar{v}_x/\partial z$ in the fluid except slab 1 and slab 11, where velocities are not differentiable. The local flow velocity in slab n, $\bar{v}_x(n)$ is determined by averaging over the particles in this slab.

$$\bar{v}_x(n) = \langle v_{x,i} \rangle, \qquad i \in \text{slab } n \tag{4}$$

The velocity profile is linear and its slope $\langle\partial\bar{v}/\partial z\rangle$ can be extracted by a linear least-squares fit. The local temperature in slab n, $T(n)$, is evaluated from peculiar velocities, i.e., the difference between the actual velocities and the local flow velocities, as eq 5

$$T(n) = \frac{1}{3N_{\text{bead}}k_{\text{B}}} \sum_{i=1}^{N_{\text{bead}}} [(v_{x,i} - \bar{v}_x(n))^2 + v_{y,i}{}^2 + v_{z,i}{}^2], \qquad i \in \text{slab } n \tag{5}$$

where k_B is Boltzmann's constant, N_{bead} is the total number of beads in slab n, m_i and v_i denote the mass and actual velocity of ith bead. The temperature profile is parabolic in both upper and lower halves of simulation cell, with cooling in the exchange

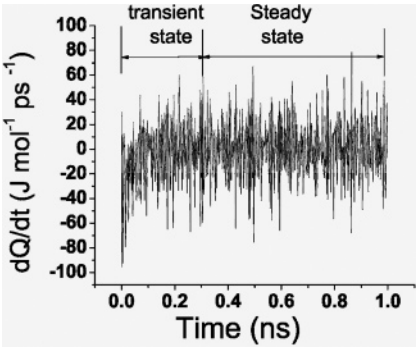

Figure 2. Evolution of the rate of heat energy (dQ/dt) input to the system by the thermostat during the simulation for PS-100 system at the highest shear rate 5.06×10^{10} s^{-1}.

slabs 1 and 11 and heating in between.[4] As the transport of momentum p_x is exactly known, the shear viscosity η at a given shear rate $\dot{\gamma} = \langle \partial \bar{v}/\partial z \rangle$ can be calculated by eq 6

$$\eta = \frac{p_x}{2tL_xL_y\langle \partial \bar{v}_x/\partial z \rangle} \tag{6}$$

The momentum flux $j_z(p_x)$ is controlled by adjusting the time elapsed between two velocity swaps $W \cdot \Delta t$. As a result, different shear rates $\dot{\gamma}$ are achieved.

It is worth considering the influence of the thermostat. As the total linear momentum and total energy are conserved, the RNEMD method, in contrast to other NEMD methods, does not need any external thermostat. However, calculations on realistic systems often necessitate a thermostat for reasons unrelated to the RNEMD scheme because either *NVT* conditions are explicitly required or temperature shifts due to round-off or cutoff noise need to be corrected. As any thermostat introduces an artificial dissipation of momentum, the calculated viscosities may carry an intrinsic error. We use an atomic version of Berendsen's thermostat,[26] i.e., the actual temperature is calculated from atomic velocities rather than center-of-mass velocities, and the atomic velocities are being rescaled. An atom-based thermostat is dictated by the system being a melt of long, flexible, and entwined polymer chains. First, in contrast to fluids of small rigid molecules, they create no problems from rotational motion, as they reorient much more slowly than they thermalize. Second, confining the temperature analysis and control only to the center-of-mass velocities (1/100 of all degrees of freedom for chain of 100 beads, namely PS-100, see Section 3) would lead to large statistical uncertainties. Finally, we need the thermostat only to counteract a very slow drift due to round-off errors. The usual main source of spurious heat generation, namely cutoff noise, plays a minor role here because our cutoff is long and the nonbonded potentials have a finite range. As the Berendsen thermostat applies a uniform scaling to all velocities, it may change velocity profiles only uniformly and only by a small amount, avoiding local artefacts. In this sense, it might have an advantage over alternative thermostats, which perform velocity scaling on an individual-atom basis.[27] In Figure 2, we report the rate of energy input into or removal from the system by the thermostat in the simulation of the biggest system (PS-100, Section 3) at the highest shear rate. It is evident that, in the steady state, the average kinetic energy added/removed by the thermostat is zero.

3. Model and Computational Technique

References 24 and 28 report, respectively, the CG model of atactic polystyrene and the corresponding force field parameters

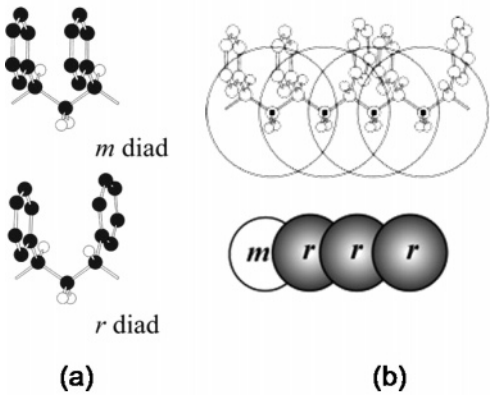

Figure 3. Illustration of the coarse-grained model of atactic polystyrene: (a) the meso (*m*) and racemo (*r*) of diads in transplanar conformation (hydrogen atoms on phenyl rings are omitted for clarity); (b) one superatom corresponding to a diadic *m* or *r* unit. The centers of these superatoms, as indicated by filled squares, are the methylene carbons. Reproduced from ref 24.

used in this work. The most important characteristics of this model are: the polystyrene diad is coarse-grained as a superatom in the mesoscale effective force field; the center of the superatom is placed at the methylene carbon; two different types of superatoms can be designated according to the configuration of two adjacent pseudoasymmetric −CHR− methyne groups, either meso (same configurations RR or SS) or racemo (opposite configurations RS or SR), as shown in Figure 3; the corresponding force-field contains three different bonds, six angles, and three nonbonded terms.

This model has been successfully tested against structural properties of polystyrene melts with different chain lengths, the dynamical behavior can be properly evaluated by taking into account the time scale.

The RNEMD simulations of monodisperse polystyrene melts are performed for four different chain lengths. Every system consists of N_{chain} polystyrene chains of N_{bead} beads, where N_{bead} is taken to be 9, 20, 30, and 100. These systems are referred to as PS-9, PS-20, PS-30, and PS-100, respectively. They are all unentangled systems. The densities of the systems are obtained from equilibrium simulations at constant temperature 500 K and constant pressure 1 atm. The relaxation time of a chain τ is obtained by time integration of the autocorrelation function for the end-to-end vector **s**, as given by eq 7

$$\tau = \int_0^\infty C(t)\,\mathrm{d}t = \int_0^\infty \langle \mathbf{s}(0)\cdot\mathbf{s}(t)\rangle / \langle \mathbf{s}^2\rangle \,\mathrm{d}t \tag{7}$$

The correlation function is noisy, so the long-time behavior is hard to take into account. To arrive at practical estimates for comparing the dynamics, we have integrated $C(t)$ until it reaches zero for the first time. The parameters of these systems are summarized in Table 1. These well-equilibrated systems are used as initial configurations of the RNEMD calculations.

All RNEMD simulations are carried out with the modified GMQ_num code, the numerical version of the molecular dynamics simulation software package GMQ.[29,30] In this modified code, orthorhombic periodic boundary conditions are applied. The simulation cells are elongated in the z direction ($L_x = L_y = L_z/3$), in which the momentum flux is imposed. The equations of motion are numerically integrated by the Verlet algorithm, the loose-coupling method of Berendsen[26] is used to control the temperature of the system, with temperature coupling time 1 ps, and neighbor lists[1] are used to speed up the computation of the nonbonded potential. The cutoff for the

Table 1. Parameters of the Coarse-Grained Model System Used[a]

system	N_{bead}	MW (g/mol)	N_{chain}	ρ (kg/m^3)	$L_x \times L_z \times Lz$ (nm)	$\langle R^2\rangle_{eq}^{1/2}$ (nm)	τ (ps)
PS-9	9	1043	150	929.8	4.534 × 4.534 × 13.602	0.549	~15
PS-20	20	2189	120	940.6	5.367 × 5.367 × 16.101	0.975	~70
PS-30	30	3230	120	945.4	6.099 × 6.099 × 18.297	1.276	~160
PS-100	100	10520	60	951.0	7.161 × 7.161 × 21.483	2.648	~2000

[a] Polymer systems, the number of beads per chain N_{bead}, the molecular weight MW, the number of chains N_{chain}, density ρ, simulation cell with size of L_x, L_y, and L_z, equilibrium root mean squared gyration radius $\langle R^2\rangle_{eq}^{1/2}$, the chain relaxation time τ.

Table 2. RNEMD Control Parameters: Length of the Time Step Δt, Velocity Swap Interval W for PS-9, PS-20, PS-30, and PS-100

PS-9		PS-20		PS-30		PS-100	
Δt (fs)	W	Δt (fs)	W	Δt (fs)	W	Δt (fs)	W
1	60	1	60	1	60	1	60
2	60	2	60	2	60	2	60
4	60	3	60	3	60	3	60
7	60	7	60	7	60	5	60
7	75	7	90	7	90	5	90
7	90	7	120	7	120	5	120
7	120	7	180	7	180	5	180
7	180	7	240	7	240	5	240
7	240	7	400	7	300	5	300
				7	347	5	330
						5	360
						5	500

nonbonded potential is $r_c = 1.5$ nm. The simulations are performed at constant temperature $T = 500$ K. The momentum flux is imposed by exchanging the x component of the velocity of beads, as described in Section 2. To cover a wide shear rate window, different velocity swap intervals $W\cdot\Delta t$ are applied: Δt is taken in the range of 1−7 fs, W in the range of every 60−500 time steps. The velocity profile sampling rate $W' = W + 1$ is in the range of every 61−501 time steps for the production runs. The velocity profiles are sampled only in those time steps in which no velocity swap is performed. Table 2 lists all the RNEMD control parameters. The system takes a certain time to reach the steady state after the perturbation is applied; this time depends on the chain length and perturbation strength. The steady state can be monitored from the time evolution of the momentum flux during the simulation, which decays to a stable average. The initial transient stage has been excluded when calculating viscosity and analyzing structural changes. The resulting shear rates for different systems are: PS-9 in the range of 1.7×10^{10}−1.3×10^{11} s^{-1}, PS-20 in the range of 1.0×10^{10}−6.6×10^{10} s^{-1}, PS-30 in the range of 5.3×10^{9}−5.7×10^{10} s^{-1}, and PS-100 in the range of 1.2×10^{9}−5.1×10^{10} s^{-1}.

It should be pointed out that the shear rates used in this work are very large compared to experiment. This results from (i) a short simulation time, compared to experimental time, and (ii) the requirement of a reasonable signal-to-noise ratio during the accessible simulation time. Lower shear rates could, in principle, be achieved by increasing the velocity swap interval $W\cdot\Delta t$ at the expense of a less well-defined temperature gradient.[4] The same is true for the algorithmic alternative of more often selecting an atom pair for exchange with a smaller velocity difference.[5] As a consequence, some of the simulations are beyond the Newtonian regime. The shear rate where shear thinning sets in can be roughly estimated as the inverse of the chain relaxation time τ^{-1},[17,18,31] for PS-9, $\tau^{-1} \sim 6.7 \times 10^{10}$; for PS-20, $\tau^{-1} \sim 1.4 \times 10^{10}$ s^{-1}; for PS-30, $\tau^{-1} \sim 6.3 \times 10^{9}$ s^{-1}; and for PS-100, $\tau^{-1} \sim 5.0 \times 10^{8}$ s^{-1}. Thus, it drastically decreases with increasing molecular weight. This is a problem common to all nonequilibrium simulations. With any method, one has to simulate long enough for polymer chains to move past each other, and one has to accumulate enough such events for a well-converged viscosity. Methods, such as the use of nonlinear response theory and transient time correlation functions have been used recently for molecular fluids such as *n*-decane[32] but are still waiting to be tried on high-molecular-weight polymers. Therefore, there are but few reports on molecular dynamics simulation of direct observation of the shear thinning onset for *realistic* polymer models, with two exceptions being the work on polyethylene chains by Padding and Briels,[18] and Kim et al.[50]

The error bar of the shear viscosity is calculated according to eq 8

$$\Delta\eta \le \langle\eta\rangle\left(\left|\frac{\Delta j_z(p_x)}{\langle j_z(p_x)\rangle}\right| + \left|\frac{\Delta\dot\gamma}{\langle\dot\gamma\rangle}\right|\right) \tag{8}$$

where $\langle\eta\rangle$ is the average viscosity, $\langle j_z(p_x)\rangle$ is the momentum flux averaged over the production run, and $\Delta j_z(p_x)$ is the standard deviation of the average $\langle j_z(p_x)\rangle$; $\langle\dot\gamma\rangle$ is the shear rate averaged over the production run, and $\Delta\dot\gamma$ is the standard deviation of the average $\langle\dot\gamma\rangle$.

4. Results and Discussion

A. Shear Viscosity and Material Functions. Here we briefly give the definition of some quantities used to analyze the results of our simulations. The apparent viscosity is calculated according to eq 1. The first and second normal stress differences $N_1(\dot\gamma)$ and $N_2(\dot\gamma)$ are calculated from diagonal elements of the stress tensor using the following equation:

$$N_1 = P_{zz} - P_{xx} \tag{9}$$

$$N_2 = P_{yy} - P_{zz} \tag{10}$$

$P_{\alpha\alpha}$ ($\alpha = x,y,z$) is calculated from the atomic implementation of virial-theorem expression:

$$P_{\alpha\alpha} = \frac{1}{V}\left(\sum_i^N m_i(v_i^\alpha - \bar v_i^{\,\alpha})^2 + \sum_i^N\sum_{j>i}^N r_{ij}^\alpha F_{ij}^\alpha\right) \tag{11}$$

where V is the volume of the simulation cell, N is the total number of beads, m_i and v_i denote the mass and actual velocity of ith bead, r_{ij} denotes the distance between bead i and j, F_{ij} is the force exerted on bead i by bead j, α refers to x, y, z components in the Cartesian coordinate system, $\bar v_i$ is the local flow velocity of ith bead, which is given by $\bar v_i = (\bar v_{x,i},0,0)$. The first and second normal stress differences $N_1(\dot\gamma)$ and $N_2(\dot\gamma)$ are presented here rather than the first and the second normal stress coefficients $\Psi_1(\dot\gamma)$ and $\Psi_2(\dot\gamma)$ ($\Psi_1 = N_1/\dot\gamma^2$, $\Psi_2 = N_2/\dot\gamma^2$), which are sometimes reported, because $N_1$and N_2 obtained from the simulations are associated with their relative errors (particularly at low shear rate) and the division of N_1 and N_2 by a very small shear rate ($\dot\gamma \to 0$) leads to large uncertainties in Ψ_1 and Ψ_2. In addition, the hydrostatic pressure P is computed from the normal stresses by eq 12

$$P(\dot{\gamma}) = \frac{1}{3}(P_{xx} + P_{yy} + P_{zz}) \tag{12}$$

Viscosity. Figure 4 shows the shear viscosity as a function of the shear rate for polymer melts with different chain lengths. For PS-9, PS-20, and PS-30, the shear viscosity functions exhibit two distinct regimes: a visible plateau at lower shear rates and a shear-thinning regime at higher shear rates. For PS-100, the shear-thinning region is dominant and the Newtonian regime is inaccessible in the given shear rate window.

The viscosity dependence on shear rate in the shear-thinning regime is often empirically described as a power-law relation, in the form $\eta \propto \dot{\gamma}^{-n}$.[33] The exponent n of the power-law can be obtained from the linear region in the log−log plot of the viscosity versus the shear rate. For comparison, the exponents obtained from this work and from some previous simulations on modeled polymers are collected in Table 3. Our results suggests that the exponent n increases with molecular weight. This dependence is more pronounced for the shorter chains (PS-9 and PS-20) than for larger molecular weights. The data qualitatively agree with Xu et al.[15] and Bosko et al.,[14] while Kröger and Hess[13] and Daivis et al.[12] found invariant exponents, and a weak shear dilatancy is detected for short chain ($N < 20$) in the work of Kröger and Hess.[13] In particular, Kröger et al.[11] show a tiny dependence on short chain lengths and almost the same exponent for longer chains. One should anyway be aware that these simulations were performed at different conditions and using different models. Moreover, the determination of the exponents is extremely sensitive to where on the shear rate curve one assumes the power-law to be valid.[14] The exponent n for PS-100 lies within the experimental values reported for polymeric liquids (n in the range 0.4−0.9).[34] The exponent derived by Doi and Edwards[35] from reptation dynamics is much higher ($n \cong 1.5$). Exponents reported from simulations are generally in the range of 0.20−0.74, which are much lower than that predicted by reptation theory. The basic assumption of reptation theory is an entangled network of polymer chains, whereas chain lengths used in simulations are often too short to form entanglements. This could be one reason for the discrepancy.

The zero-shear viscosity η_0 is of both theoretical and industrial interest. It is defined as the melt viscosity in the limit of $\dot{\gamma} \to 0$, and it is a function of temperature and molecular weight. Because in molecular dynamics, simulation of very low shear rates are not accessible for complex liquids, the way to extrapolate the data to low shear rates becomes a key issue when estimating the η_0. The extrapolation schemes used in previous simulation are not entirely consistent. Cummings et al.[36] evaluated the η_0 for liquid rubidium by using the scheme $\eta = \eta_0 - A\dot{\gamma}^{1/2}$, which is based on the mode-coupling theory of Kawasaki and Gunton.[37] Evans and Morriss[2] confirm this theoretical prediction via NEMD simulation for the triple-point Lennard-Jones fluid. However, this $\dot{\gamma}^{1/2}$ dependence of shear viscosity has not been confirmed for complex molecular fluids. Moreover, for recent work questions such dependence,[38−40] Daivis et al.[12] evaluated the η_0 for the modeled polymer by the extrapolation scheme $\eta = \eta_0 - A\dot{\gamma}^2$, which is based on the retarded motion expansion (RME) for a third-order fluid. Bosko et al. determined the η_0 for the dendrimer by taking the average of several extrapolation schemes.[14] As RME offers a systematic and model-independent description of an arbitrary viscoelastic fluid at low shear rates,[41] it would be reasonable to evaluate the η_0 of the polymer by the $\eta = \eta_0 - A\dot{\gamma}^2$ scheme. The η_0 value of polymers has also been obtained from experimental work by the extrapolation scheme $\log(\eta^{-1}) = \log(\eta_0^{-1}) - A\tau_{xz}$,[42−44] where τ_{xz} is the off-diagonal component (xz) of the stress tensor. In this work, the η_0 is determined as an average of values by using two different extrapolation schemes, as demonstrated for the case of PS-9 in Figure 5: (1) $\eta = \eta_0 - A\dot{\gamma}^2$ and (2) $\log(\eta^{-1}) = \log(\eta_0^{-1}) - A\tau_{xz}$. For the latter extrapolation, we use the momentum flux $|j_z(p_x)|$ instead of the shear stress τ_{xz}. The η_0 determined for all systems are summarized in Table 4, except for PS-100, because the given shear rate window for PS-100 is unable to reach the Newtonian regime. The η_0 determined by these two extrapolation schemes agree well with each other in the uncertainty limit. The dependence of η_0 on the molecular weight is linear ($\eta_0 \propto M$) for short chains.[45] Such dependence on the molecular weight is predicted by the Rouse model. As shown in Figure 6, one observes an almost linear dependence of η_0 on the molecular weight, with the slopes of 0.98 and 1.10 obtained from both extrapolation schemes.

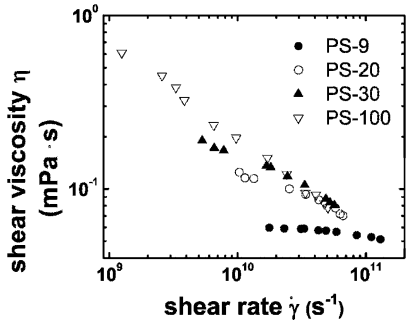

Figure 4. Shear-rate dependence of the shear viscosity for PS-9, PS-20, PS-30, and PS-100. Error bars are approximately the same size as the symbols and have been omitted for clarity.

Experiment[46] indicates that the zero-shear viscosity for polystyrene of molecular weight ∼1000 g/mol at 500 K is around15 × 10^{-3} Pa·s. Comparing the η_0 for the similar molecular weight of PS-9 in this work, the simulation result (∼0.06 × 10^{-3} Pa·s) is much lower than the experiment, by a factor of ∼250. As predicted by hydrodynamics, the zero-shear viscosity and the self-diffusion coefficient are approximately reciprocal.[47] The self-diffusion coefficient of the coarse-grained model used in this work is, indeed, found to be a factor of ∼200 higher than that of the fully atomistic model of the PS-9 system.[24] Therefore, the difference of the zero-shear viscosity between simulation and experiment can be traced mainly to the fast dynamics of the coarse-grained model used. There could be two possible explanations: (1) The reduction of the number of degrees of freedom upon coarse-graining eliminates the fluctuating force associated with those missing molecular degrees of freedom.[48] (2) The coarse-grained force field is generally very soft. This leads to the reduction of nearest-neighbor interactions, particularly of their repulsion, and thereby atoms can more easily escape from the local cages formed by their neighbors.[25] According to Boltzmann's superposition principle, the zero-shear viscosity can be deduced from the time-dependent shear modulus $G(t)$,[49] i.e.,

$$\eta_0 = \int_0^\infty G(t)\,\mathrm{d}t \tag{13}$$

Hence, the fast dynamics of the coarse-grained model can affect η_0 through the shear modulus. Two parts contribute to the shear modulus in an unentangled system[49]

$$G(t) = G_{\mathrm{mic}}(t) + G_{\mathrm{Rouse}}(t) \tag{14}$$

The first term $G_{\mathrm{mic}}(t)$ accounts for the short-time behavior, which is controlled by the internal degrees of freedom or microstruc-

Table 3. Exponent n of the Power Law ($\eta \propto \dot{\gamma}^{-n}$) in the Shear Thinning Region for Different Chain Length N_{bead} from This Work and Some Other Conventional NEMD Simulations[a]

author	model	force field	ensemble and density	exponent n (chain-length N_{bead})
this work	realistic linear polymer	coarse-grained force field contains three different bonds, six angles and three nonbonded terms for the nonbonded part	*NVT* different densities for different chain lengths	0.12 ± 5.2% ($N = 9$) 0.34 ± 5.6% ($N = 20$) 0.43 ± 6.0% ($N = 30$) 0.56 ± 7% ($N = 100$)
Xu. et al.[b]	model linear chain	LJ for any two beads interaction and FENE potential used for adjacent beads interaction	*NVT* same density for different chain lengths	0.25 ($N = 10$) 0.35 ($N = 20$) 0.42 ($N = 50$)
Kröger et al.[c]	model linear chain	all beads interact with a repulsive LJ and FENE potential is added for adjacent beads along a chain interaction	*NVT* same density for different chain length	0.30 ($N = 10$) 0.45 ($N = 30$) 0.46 ($N = 60$) 0.47 ($N = 100$)
Bosko et al.[d]	model linear chain	WCA potential for all two beads interaction, FENE potential for adjacent beads along a chain interaction	*NVT* same density for different chain lengths	0.321 ± 2% ($N = 19$) 0.413 ± 5% ($N = 43$) 0.523 ± 2% ($N = 91$) 0.743 ± 3% ($N = 187$)
Daivis et al.[e]	model linear chain	WCA potential for all two beads interaction except the those that are bonded to each other within a molecule, rigidly constrained bonds	*NVT* same density for different chain lengths	0.45 ($N = 4$) 0.43 ($N = 10$) 0.42 ($N = 20$) 0.45 ($N = 50$)
Kröger and Hess[f]	model linear chain	all beads interact with a repulsive LJ and FENE potential is added for adjacent beads along a chain interaction	*NVT* same density for different chain length	0.60 ± 0.10 ($N = 20\sim400$) weak shear dilatancy ($N < 20$)

[a] LJ potential refers to Lennard-Jones potential, WCA potential refers to Weeks−Chandler−Anderson potential, FENE potential refers to finitely extensible nonlinear elastic potential. [b] Ref 15. [c] Ref 11. [d] Ref 14. [e] Ref 12. [f] Ref 13.

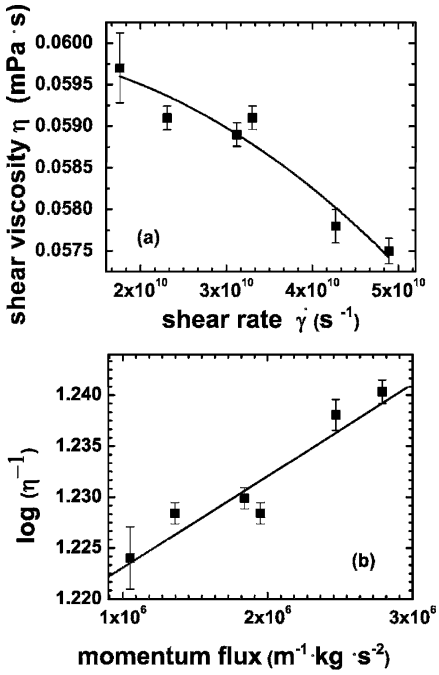

Figure 5. Demonstration of the extrapolation schemes used to obtain the zero-shear viscosity from simulation for the PS-9 system: (a) scheme 1: $\eta = \eta_0 - A\dot{\gamma}^2$ (b) scheme 2: $\log(\eta^{-1}) = \log(\eta_0^{-1}) - A|j_z(p_x)|$.

Table 4. Estimated Values of the Zero-Shear Viscosity (η_0) by the Different Extrapolation Scheme (1) $\eta = \eta_0 - A\dot{\gamma}^2$, (2) $\log(\eta^{-1}) = \log(\eta_0^{-1}) - A|j_z(p_x)|$

extrapolation scheme	PS-9 (mPa · s)	PS-20 (mPa · s)	PS-30 (mPa · s)
1	0.060 ± 0.3%	0.122 ± 0.5%	0.182 ± 2%
2	0.061 ± 8.0%	0.148 ± 10%	0.208 ± 12%

ture. This contribution cannot be reproduced well by a coarse-grained model because short-time degrees have been eliminated in order to improve the computational efficiency. The second term $G_{Rouse}(t)$ accounts for the generic Rouse dynamics, which

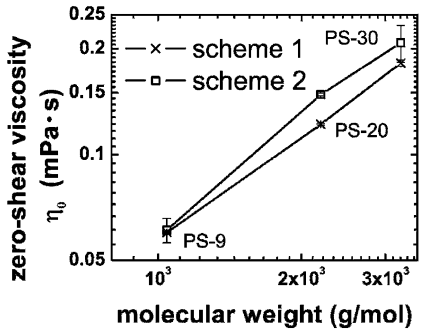

Figure 6. Zero-shear viscosity versus molecular weight. Data used from extrapolation scheme (1) $\eta = \eta_0 - A\dot{\gamma}^2$, (2) $\log(\eta^{-1}) = \log(\eta_0^{-1}) - A|j_z(p_x)|$. The slopes of linear fits for these data are 0.98 ± 0.1%, 1.10 ± 0.3%, respectively. Solid lines are used to guide eyes.

can be reproduced by the coarse-grained model by taking into account a time scale factor. Both terms complicate the viscosity prediction in the coarse-grained model, and for details, a further study is required. Still, the agreement of η_0 with Rouse theory and experiment is encouraging when the time scale factor is taken into account.

Normal Stress Difference. As in experimental[33] and previous NEMD simulation data,[15,19] the first normal stress difference N_1 predicted from this work is positive for all cases, as shown in Figure 7. This validates the theoretical prediction that simple shear is accompanied by a nonvanishing normal stress difference.[49] Physically, this corresponds to a compressing force perpendicular to the plane in which shear flow take place.

As the shear rate increases, N_1 increases significantly, following a power-law in the shear-thinning region in the form: $N_1 \propto \dot{\gamma}^{\alpha}$ (For PS-9, 20, 30, 100, α = 1.0, 0.72, 0.66, 0.53, respectively). A similar behavior has been observed for polyethylene by Jabbarazadeh et al. in their NEMD simulation.[19] Concerning the second normal stress difference N_2, both experimental and simulation work provide only limited data. However, it has been pointed out[33] based on experimental findings that N_2 is negative for homogeneous polymer liquids,

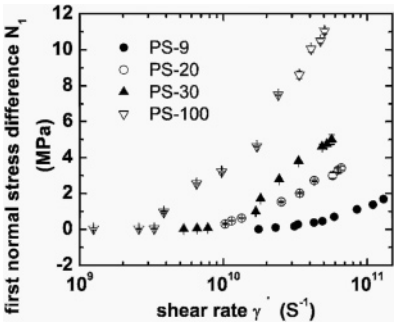

Figure 7. First normal stress difference N_1 versus shear rate $\dot{\gamma}$ for polystyrene melts of PS-9, PS-20, PS-30, and PS-100.

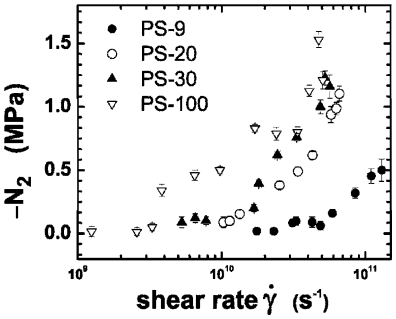

Figure 8. Second normal stress difference N_2 versus shear rate $\dot{\gamma}$ for polystyrene melts of PS-9, PS-20, PS-30, and PS-100.

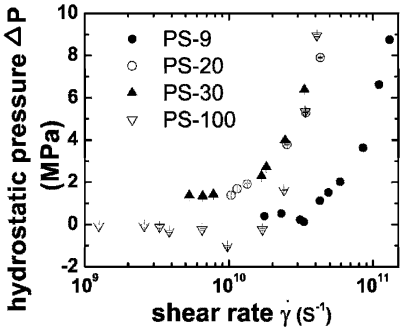

Figure 9. Hydrostatic pressure difference $\Delta P = P(\dot{\gamma}) - P(0)$ versus shear rate for polystyrene melts of PS-9, PS-20, PS-30, and PS-100.

that $-N_2/N_1$ typically lies in the range 0.2−0.3, and that it is insensitive to the shear rate. Figure 8 indicates that N_2 is negative for nearly all the systems and it increases with the shear rate in the shear-thinning region. The values of $-N_2/N_1$ in the shear-thinning region for PS-9, 20, and 30 are in the range of 0.2−0.3; for PS-100, it is 0.1−0.2.

Hydrostatic Pressure. Figure 9 shows the dependence of the hydrostatic pressure on the shear rate. Two different regimes are visible. At higher shear rate, the hydrostatic pressure increases with the shear rate, and it seems again to follow the power-law $P = P_0 + \dot{\gamma}^{\beta}$. Similar behavior was found for polyethylene[17,19] and dendrimers.[14] At lower shear rate, there is a small, if any, increase of the hydrostatic pressure, and it is close to the equilibrium value. Moore et al.[17] have found a minimum of the hydrostatic pressure before a rapid increase, and this pressure minimum occurs at the same shear rate in which the intermolecular LJ potential energy has a minimum. Because of uncertainty at the low shear rate in our result, the existence of such a minimum can neither be confirmed nor ruled out.

B. Structural Alteration under Shear. The dependence of the molecular configurations and alignment on the shear rate is covered in this section. In the following analyses, the molecules,

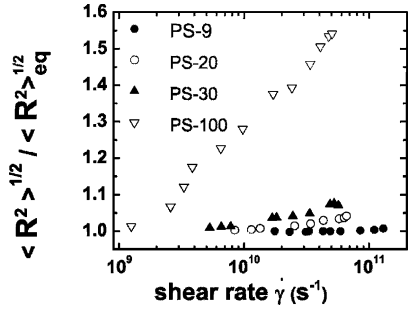

Figure 10. Root mean squared gyration radius, $\langle R^2\rangle^{1/2}$, versus shear rate for PS-9, PS-20, PS-30, and PS-100. $\langle R^2\rangle^{1/2}$ is normalized by its equilibrium value $\langle R^2\rangle^{1/2}_{eq}$ (no shear).

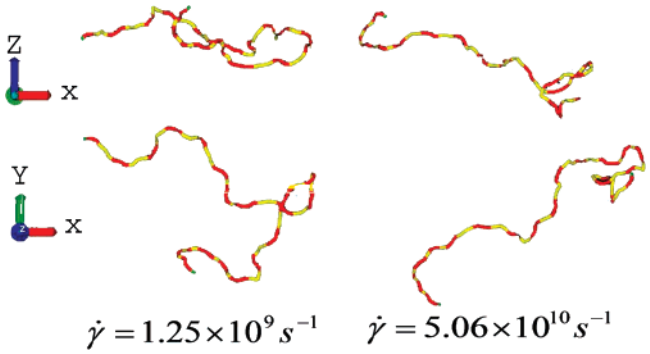

Figure 11. Typical configurations of individual chains of PS-100 under different shear rates.

whose centers of mass are in the velocity-exchange slabs (slab1 and slab 11), have been excluded.

Average Chain Dimension. Figure 10 shows the root mean squared gyration radius $\langle R^2\rangle^{1/2}$ as a function of the shear rate for different chain lengths. Figure 11 shows the configurations of a single chain of PS-100 under different shear rate. At low shear rates, $\langle R^2\rangle^{1/2}$ approaches its equilibrium value. As the shear rate increases, the shear field deforms the configuration and elongates the chain. These changes are more marked for the long chains.

Shear-Induced Alignment. Shear-induced alignment is investigated in term of birefringence extinction angle χ. As in RNEMD, the flow field imposed on the system corresponds to two symmetric planar Couette flows; the momentum fluxes $j_z(p_x)$ in the upper and lower halves are equal in magnitude but opposite in direction. Both half cells have the same shear rate, but the velocity profiles are symmetric. As a consequence, polymer chains are aligned symmetrically in the two halves of the simulation cell. This is found, indeed, in the distribution of the single-molecule alignment angle θ, the angle between the end-to-end vector, and the flow direction x, as shown for the case of PS-30 in Figure 12. Therefore, the birefringence extinction angle χ should be calculated from both halves of the cell separately. One can take the average of χ from both half cells to improve the statistics.

To describe the shear-induced alignment, we calculate an order tensor **S** defined in eq 15

$$\mathbf{S} = \frac{1}{N}\left\langle \sum_{i=1}^{N}\left(\mathbf{u}_i \otimes \mathbf{u}_i - \frac{1}{3}\mathbf{I}\right)\right\rangle \tag{15}$$

where, $\mathbf{u}_i$ is the unit vector along the end-to-end direction of the molecule i, and **I** is the unit tensor. The angle brackets indicate an ensemble average. The birefringence extinction angle χ is calculated as the angle between the eigenvector of **S**

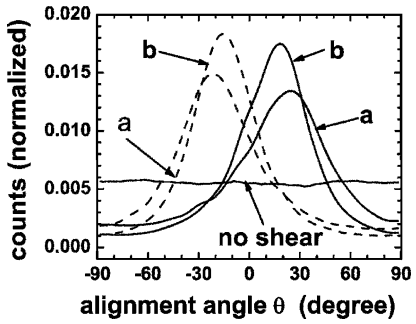

Figure 12. Distributions of the single molecule alignment angle θ at various shear rates $\dot{\gamma}$ for the PS-30 system. The solid lines are from the upper half of the simulation cell, the dashed lines from the lower half. The distribution is weighted by a factor of $1/\sin\theta$. For (a) shear rate $\dot{\gamma} = 1.82 \times 10^{10}$ s^{-1}, the distribution maxima obtained from the upper and lower halves of the simulation cell are 22.9° and −22.0°, respectively. For (b) shear rate $\dot{\gamma} = 3.34 \times 10^{10}$ s^{-1}, the maxima are 16.5° and −16.1°, respectively.

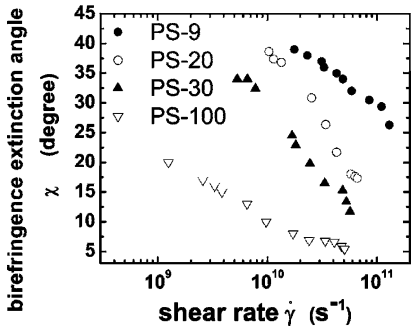

Figure 13. Birefringence extinction angle χ as a function of the shear rate for PS-9, PS-20, PS-30, and PS-100.

corresponding to the largest eigenvalue of the order tensor and the shear flow direction *x*.

As shown in Figure 13, the birefringence extinction angle decreases as the shear rate increases. These changes describe quantitatively the alignment of the system with respect to the flow direction. The process of chain alignment, in combination with chain stretching, leads to a macroscopic anisotropy of the material. It is expected that the birefringence extinction angle converges to 45° in the Newtonian regime.[35] The birefringence extinction angles of PS-9 and PS-20 system at low shear rates are close to 45°, but the birefringence extinction angle of PS-100 is still far from 45°. This indicates again that the shear rates used in this work are not low enough to reach the Newtonian regime for the long chains. Note that, for PS-100 at the highest shear rate of $\dot{\gamma} = 5.06 \times 10^{10}$ s^{-1}, the root mean squared gyration radius $\langle R^2\rangle^{1/2}$ is larger than the half length of the simulation cell ($L_x/2$ and $L_y/2$), and the finite box size limits the minimum flow alignment angle to around 5°.

5. Summary

The RNEMD method has been used to calculate the viscosity of a coarse-grained model of short-chain polystyrene. The simulations were performed at constant temperature and constant volume. The viscometric functions obtained in this paper can be summarized as follows: (1) The zero-shear viscosity is linearly dependent on the molecular weight for PS-9, PS-20, and PS-30 systems; this agrees with experiments and the theoretical prediction of the Rouse model. (2) The shear-thinning behavior for all studied systems follows a power law. The exponent of the power law increases with the molecular weight, and this dependence is more pronounced for short chains (PS-9 and PS-20). (3) The first normal stress difference is positive, and the second normal stress is negative for all systems. The first normal stress difference follows the power law of form of $N_1 \propto \dot{\gamma}^{\alpha}$ at higher shear rates. (4) The hydrostatic pressure increases at higher shear rates. The structural changes under shear are quantitatively investigated. The analysis of these effects indicates that the process of chain alignment, in combination with chain stretching, leads to a macroscopic anisotropy of the material. The reverse nonequilibrium molecular dynamics method gives reliable results in the Newtonian regime and a still-reasonable agreement with homogeneous-shear NEMD methods at higher shear rates. As other methods, it has problems when the shear rates are extremely high.

The extrapolated zero-shear viscosity is linearly dependent on the molecular weight even though its absolute value is lower than the experiments by a factor of ∼200 for the shortest chain length. This scaling factor is probably due to the well-known intrinsic speed up of the coarse-grained model. The scaling factor found for the viscosity is close to that of the diffusion coefficient calculated from equilibrium MD simulations of the same model. This result indicates that the CG model which has been developed by taking only structural information into account can reproduce the generic Rouse behavior, and those short-time degrees which have been actively removed in the CG model are responsible for the larger difference of zero-shear viscosity between simulation and experiment.

Acknowledgment. We are indebted to Prof. David Brown and Dr. Sévérine Queyroy, Université de Savoie, for providing the GMQ_num code and to Dr. Max Rüllmann, BASF AG, for the experimental reference data. This work has been supported by the Deutsche Forschungsgemeinschaft, the German Ministry of Education and Research (BMBF), and the Alexander-von-Humboldt Foundation.

References and Notes

(1) Allen, M. P.; Tildesley, D. J. *Computer Simulation of Liquids*; Oxford University Press: New York, 1987.
(2) Evans, D. J.; Morriss, G. P. *Statistical Mechanics of Nonequilibrium Liquids*; Academic Press: London, 1990.
(3) Hess, B. *J. Chem. Phys.* **2002**, *116*, 209−217.
(4) Müller-Plathe, F. *Phys. Rev. E* **1999**, *59*, 4894−4898.
(5) Müller-Plathe, F.; Bordat, P. Reverse Non-Equilibrium Molecular Dynamics. In *Lect. Notes Phys.* **2004**, *640*, 310−326.
(6) Soddemann, T., Ph.D. Thesis, Johannes Gutenberg-Universität Mainz, Germany 2001.
(7) Bordat, P.; Müller-Plathe, F. *J. Chem Phys.* **2002**, *116*, 3362−3369.
(8) Guo, H.; Kremer, K.; Soddemann, T. *Phys. Rev. E* **2002**, *66*, 061503.
(9) Soddemann, T.; Auernhammer, G. K.; Guo, H.; Dünweg, B.; Kremer, K. *Eur. Phys. J. E* **2004**, *13*, 141−151.
(10) Donkó, Z.; Goree, J.; Hartmann, P.; Kutasi, K. *Phys. Rev. Lett.* **2006**, *96*, 145003.
(11) Kröger, M.; Loose, W.; Hess, S. *J. Rheol.* **1993**, *37*, 1057−1079.
(12) Daivis, P. J.; Matin, M. L.; Todd, B. D. *J. Non-Newtonian Fluid Mech.* **2003**, *111*, 1−18.
(13) Kröger, M.; Hess, S. *Phys. Rev. Lett* **2000**, *86*, 1128−1131.
(14) Bosko, J. T.; Todd, B. D.; Sadus, R. J. *J. Chem. Phys.* **2004**, *121*, 12050−12059.
(15) Xu, Z.; de Pablo, J. J.; Kim, S. *J. Chem. Phys.* **1995**, *102*, 5836−5844.
(16) Kröger, M. *Phys. Rep.* **2004**, *390*, 453−551.
(17) Moore, J. D.; Cui, S. T.; Cochran, H. D.; Cummings, P. T. *J. Non-Newtonian Fluid Mech.* **2000**, *93*, 83−99.
(18) Padding, J. T.; Briels, W. J. *J. Chem. Phys.* **2003**, *118*, 10276−10286.
(19) Jabbarzadeh, A.; Atkinson, J. D.; Tanner, R. I. *Macromolecules* **2003**, *36*, 5020−5031.
(20) Padding, J. T.; Briels, W. J. *J. Chem. Phys.* **2001**, *115*, 2846−2859.
(21) Akkermans, R. L. C.; Briels, W. J. *J. Chem. Phys.* **2000**, *113*, 6409−6422.
(22) Fukunaga, H.; Takimoto, J.; Doi, M. *J. Chem. Phys.* **2002**, *116*, 8183−8190.
(23) Kremer, K.; Müller-Plathe, F. *MRS Bull.* **2001**, *26*, 205−210.
(24) Milano, G.; Müller-Plathe, F. *J. Phys. Chem. B* **2005**, *109*, 18609−18619.

(25) Depa, P. K.; Maranas, J. K. *J. Chem. Phys.* **2005**, *123*, 094901.
(26) Berendsen, H. J. C.; Postma, J. P. M.; van-Gunsteren, W. F.; DiNola, A.; Haak, J. R. *J. Chem. Phys.* **1984**, *81*, 3684−3690.
(27) Zhang, M.; Lussetti, E.; Souza, L. E. S. d.; Müller-Plathe, F. *J. Phys. Chem. B* **2005**, *109*, 15060−15067.
(28) Spyriouni, T.; Tzoumanekas, C.; Theodorou, D.; Müller-Plathe, F.; Milano, G. *Macromolecules* **2007**, *40*, 3876.
(29) Brown, D. *The GMQ Manual*, Version 3; http://uni-savioe.fr/labos/mops/brown/gmq.html, 1999.
(30) Queyroy, S. Simulations moléculaires dynamiques de surfaces de polymère amorphe: cas de la cellulose. Ph.D. Thesis, Université de Savoie, 2004.
(31) Cui, S. T.; Cummings, P. T.; Cochran, H. D.; Moore, J. D.; Gupta, S. A. *Int. J. Thermophys.* **1998**, *19*, 449−459.
(32) Pan, G.; McCabe, C. *J. Chem Phys.* **2006**, *125*, 194527.
(33) Mark, J.; Ngai, K.; Graessley, W.; Mandelkern, L.; Samulski, E.; Koenig, J.; Wignall, G. *Physical Properties of Polymers*, 3rd ed.; Cambridge University Press: New York, 2004.
(34) Bird, R. R.; Curtis, C. F.; Armstrong, R. C.; Hassager, O. *Dynamics of Polymeric Liquids, Fluid Mechanics*; John Wiley & Sons: New York, 1987, Vol. 1.
(35) Doi, M.; Edwards, S. F. *The Theory of Polymer Dynamics*; Oxford University Press: New York, 1988.
(36) Cummings, P. T.; Morriss, G. P. *J. Phys. F* **1987**, *17*, 593−604.
(37) Kawasaki, K.; Gunton, J. D. *Phys. Rev. A* **1973**, *8*, 2048−2064.
(38) Ryckaert, J.-P.; Bellemans, A.; Ciccotti, G.; Paolini, G. V. *Phys. Rev. Lett.* **1988**, *60*, 128−131.
(39) Pierleoni, C.; Ryckaert, J.-P. *Phys. Rev. A* **1991**, *44*, 5314−5317.
(40) Todd, B. D. *Phys. Rev. E* **2005**, *72*, 041204.
(41) Bird, R. R.; Curtis, C. F.; Armstrong, R. C.; Hassager, O. *Dynamics of Polymeric Liquids, Kinetic Theory*, 2nd ed.; John Wiley & Sons: New York, 1987; Vol. 2.
(42) Spencer, R. S.; Dillon, R. E. *J. Colloid Sci.* **1948**, *3*, 163−180.
(43) Spencer, R. S.; Dillon, R. E. *J. Colloid Sci.* **1949**, *4*, 241−255.
(44) Vinogradov, G. V.; Malkin, A. Y. *J. Polymer Sci., Part A: Polym. Chem.* **1964**, *2*, 2357−2372.
(45) Bicerano, J. *Prediction of Polymer Properties*, revised and expanded, 2nd ed.; Marcel Dekker: New York, 1996.
(46) Viscosity data of short-chain polystyrene (1000 g/mol) measured at 80 °C (207.3 Pa s), 110 °C (2.9 Pa s), 130 °C (0.57 Pa s), and 145 °C (0.23 Pa s) were extrapolated to 500 K using the Williams−Landel−Ferry equation. The experimental data were provided by BASF AG (M. Rüllmann, personal communication).
(47) Phillies, G. D. J. *Macromolecules* **2002**, *35*, 7414−7418.
(48) Izvekov, S.; Voth, G. A. *J. Chem. Phys.* **2006**, *125*, 151101.
(49) Strobl, G. R. *The Physics of Polymers: Concepts for Understanding Their Structures and Behavior*; Springer-Verlag: New York, 1996.
(50) Kim, J. M.; Keffer, D. J.; Kröger, M.; Edwards, B. J. *J. Non-Newtonian Fluid Mech.*, in press.

MA0707178